Corrosion Science 268 (2026) 113909

Contents lists available at ScienceDirect

Corrosion Science

journal homepage: www.elsevier.com/locate/corsci

Predictive modeling of cyclic oxidation in high-temperature alloys enabled by thermodynamics-informed machine learning

Haoyi Xu [a,b,1], Xiaoyu Sun [a,1], Guanshui Ma [a], Zhenyu Wang [a], Xin Yu [d], Liang Jiang [c], Aiying Wang [a,b,*]

[a] State Key Laboratory of Advanced Marine Materials, Zhejiang Key Laboratory of Extreme-environmental Material Surfaces and Interfaces, Ningbo Institute of Materials Technology and Engineering, Chinese Academy of Sciences, Ningbo 315201, China
[b] Center of Materials Science and Optoelectronics Engineering, University of Chinese Academy of Sciences, Beijing 100049, China
[c] Institute for Advanced Studies in Precision Materials, Yantai University, Yantai, Shandong 264005, China
[d] School of Materials Science and Engineering, Central South University, Changsha 410083, China

ARTICLE INFO

Keywords:
Machine learning
Cyclic oxidation
Ni-based alloys
Physics-informed
SHAP analysis

ABSTRACT

Prediction of cyclic oxidation performance in nickel-based alloys still remains great challenging due to its complex and nonlinear kinetics under harsh high-temperature conditions. Here, we established a thermodynamics-informed machine learning (ML) framework to estimate cyclic oxidation kinetics of superalloys by integrating thermodynamics descriptors with compositional and experimental parameters. Among six regression algorithms evaluated, a Bayesian-optimized XGBoost model achieves high predictive accuracy, with independent test R^2 exceeding 0.83. Further, SHAP analysis identifies cycle number (22.3% relative importance) and the Gibbs free energy of Al_2O_3 formation (17.3%) as primary drivers, with Al content (10.6%) and the Al+Cr descriptor underscoring the critical role of protective alumina formation and Al-Cr synergy. The framework further enables high-throughput screening of compositional space, accelerating the rational design of high-performance alloys for extreme oxidizing environments.

1. Introduction

High-temperature alloys are widely employed to manufacture the hot-section components in modern aircraft engines and industrial gas turbines [1–4]. If unimpeded, the oxidizing atmosphere at elevated temperatures can quickly render the materials failure. Usually, these materials form dense, slow-growing, and adherent oxide scales, such as Al_2O_3 and/or Cr_2O_3, against further oxidation [5–7]. Unfortunately, these protective physic barriers can be destroyed by the stress concentration, surface rumpling and elemental degradation during their long-term serve process. Although the foundations of oxidation science had been laid in early 1930s by Carl Wagner [8] and further supplemented by subsequent researchers [9–14], it is still a grand challenge to accurately predict oxidation resistance for these multi-component systems.

The oxidation of high-temperature alloys is a spontaneous chemical reaction with environment forming oxides in a selective manner, accompanied by multi-component diffusion and the peeling-off of oxides. In previous research, Ni-Al-Cr oxidation maps were constructed based on experimental tests, determining the Al and/or Cr thresholds for the formation of protective oxide layers [15,16]. Predicated on the Wagner' theories, a thermodynamic criterion was proposed to predict the oxidation performance of superalloy. The thermodynamic approach markedly improves the prediction efficiency, but it is unable to comprehensively explore the vast composition space, limited by the existing database and the time cost.

Recently, machine learning (ML) was employed as a transformative tool in the oxidation study. This data-driven method excels in capturing complex, non-linear relationships between alloy composition, processing parameters, and oxidation kinetics, thereby providing insights that are often elusive with traditional models [17–22]. Typically, Bayesian Neural Networks incorporated uncertainty quantification to automatically rank element effects on the oxidation performance of alloys [23], while CNN-LSTM models captured temporal dynamics in oxidation

* Corresponding author at: State Key Laboratory of Advanced Marine Materials, Zhejiang Key Laboratory of Extreme-environmental Material Surfaces and Interfaces, Ningbo Institute of Materials Technology and Engineering, Chinese Academy of Sciences, Ningbo 315201, China.
E-mail address: aywang@nimte.ac.cn (A. Wang).
[1] these authors contributed equally to this work.

https://doi.org/10.1016/j.corsci.2026.113909
Received 19 February 2026; Received in revised form 16 April 2026; Accepted 5 May 2026
Available online 6 May 2026

kinetics, providing accurate activation energy estimates beyond parabolic law assumptions [24]. Beyond neural networks, tree-based models were applied to predict oxide scale thickness [25] and k_p [26,27] with high efficiency, as well as to guide the compositional design of oxidation-resistant high-entropy alloys by identifying critical elemental thresholds [28], significantly accelerating the inverse design of new materials. However, existing ML models have primarily focused on isothermal oxidation, with far less attention given to cyclic oxidation, despite the latter being more relevant to the practical service conditions of high-temperature alloys. In contrast to isothermal oxidation, cyclic oxidation involves repeated heating and cooling, inducing thermal stress, oxide cracking, interfacial damage, and scale spallation. Therefore, the degradation process arises from the interplay of oxide growth and repeated scale failure and re-growth, highlighting the importance of predicting the dynamic weight-change response under cyclic conditions.

In this research, we established a thermodynamics-informed machine learning framework to predict the cyclic oxidation performance of nickel-based high-temperature alloys. By systematically integrating thermodynamic descriptors with composition and experimental parameters, and leveraging a large-scale database, the model achieves high predictive accuracy ($R^2 > 0.83$) at 1100 °C. Advanced SHAP analysis reveals the nonlinear synergistic effects of key elements like Al and Cr. Collectively, this work bridges data-driven prediction with physical mechanisms, significantly reducing experimental dependency and accelerating alloy screening, which brings forward a new paradigm to design oxidation-resistant high-temperature alloys.

2. Methods

2.1. Data collecting and preprocessing

Fig. 1 illustrates the overall workflow, encompassing three integrated phases of ML modeling, validation and interpretation. The present dataset was collected from a public cyclic oxidation database [29], comprising approximately 3000 commercial and laboratory-prepared alloys corresponding to 40803 data records. This research addressed on the Ni-based alloys containing Al, that helped establish a dense alumina layer in conferring oxidation resistance.

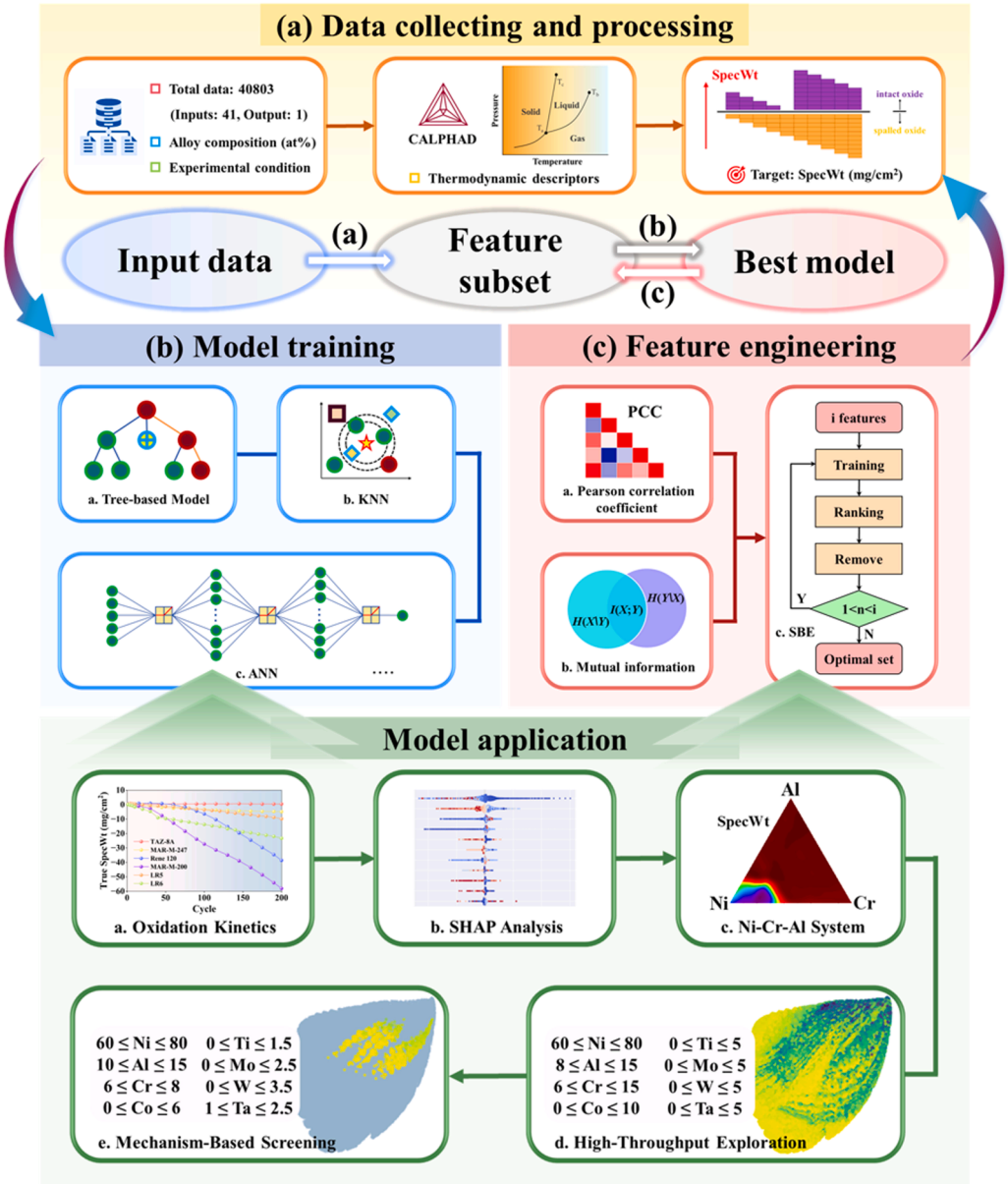

Fig. 1. The workflow of the physics-informed machine learning (ML) approach.

Based on the established oxidation theories [15,30], a feature set (as detailed in Table 1) was constructed as the input parameters of the ML model, including the experimental conditions (temperature, cycle count), the alloy compositions, the ratio of Cr/Al and their sum, and the thermodynamic features including the Gibbs free energy of Al_2O_3 formation (ΔG_f), the activity of Al and Cr, and total effective valence (Val^{eff}). Thereinto, each cycle comprised heating, 1 h dwell at target temperatures and following cooling. The specific weight change (SpecWt, ΔW/A, in mg/cm^2) during cyclic oxidation was employed as the key prediction target.

Thus far, to mitigate the influence of scale differences, the input features were normalized using the Z-score method:

$$z_i = \frac{x_i - \mu}{\sigma} \tag{1}$$

where x_i is the original feature value and z_i is the normalized value. μ and σ represents the mean and standard deviation of the features across the dataset, respectively.

Fig. 2 exhibits the distribution of SpecWt, which behaviors a pronounced negative skewness (approximately −4.994) with a heavy left tail, reflecting that the data are clustered near zero with a long tail extending towards substantial mass loss. The distributions of input features within the dataset are further provided in Supplementary Fig. S1. Overall, the dataset is dominated by conventional Ni-based superalloy chemistries, while the coverage of some minor or rare elements remains relatively limited. In particular, the coverage of Cu, Hf, Y, Th, Mn, V, N, O, La, Re, Pt, Ce, Misch, Sm, Er, Gd, Ga, Ru, and Pd is below 10% in the database. Therefore, the statistical significance of these elements in the present model is limited, and caution is needed when interpreting their individual effects.

2.2. Feature engineering and modeling

An initial feature selection was performed to mitigate potential redundancy in the feature set prior to subsequent engineering steps. The Pearson correlation coefficient (PCC) was first calculated to assess linear relationships among the 41 initial features. The correlation matrix is visualized in Fig. 3a, which provides a comprehensive heatmap of the pairwise PCC values. This analysis helps identify multicollinearity and linear dependencies between features.

Based on the PCC analysis, a threshold of $|PCC| > 0.9$ was applied to identify and address multicollinearity [31,32], as detailed in Supplementary Table S1. Fig. 3b illustrates the top 10 features ranked by their absolute PCC values with SpecWt. However, all these values are generally below 0.2, indicating weak linear associations between these features and the SpecWt. It means that the current dataset cannot be simply described by linear correlations.

Table 1
41 Initial input features for ML models, corresponding descriptions, and calculation formula.

Feature	Description	Formula
ΔG_f	Thermodynamic driving force for Al_2O_3 formation	$\Delta G_f = \Delta G_0 + RT\ln\left(\frac{a_{M_xO_y}^{2/y}}{a_M^{2x/y}\cdot P_{O_2}}\right)$
Val^{eff}	Net effect of impurities on Al_2O_3 defect chemistry	$\mathrm{Val}^{\mathrm{eff}} \equiv \sum_i (z_i - z_{\mathrm{Al}})\bar{c}_i$
a_{Al}	Effective concentration of Al for reaction	$a_{\mathrm{Al}} = \gamma_{\mathrm{Al}} \cdot X_{\mathrm{Al}}$
a_{Cr}	Effective concentration of Cr for reaction	$a_{\mathrm{Cr}} = \gamma_{\mathrm{Cr}} \cdot X_{\mathrm{Cr}}$
Al+Cr	Sum of Al and Cr	Al + Cr
Cr/Al	Ratio of Al and Cr	$\frac{\mathrm{Cr}}{\mathrm{Al}}$
Temp	Cyclic oxidation temperature	—
Cycle	Number of oxidation cycles	—
Fe, Ni, Co, Cr, Cu, Al, Ti, Hf, Zr, Y, Mo, W, Ta, Nb, Th, C, Si, Mn, V, B, N, O, La, Re, Pt, Ce, Misch, Sm, Er, Gd, Ga, Ru, Pd	Atomic percentage of 33 elements	

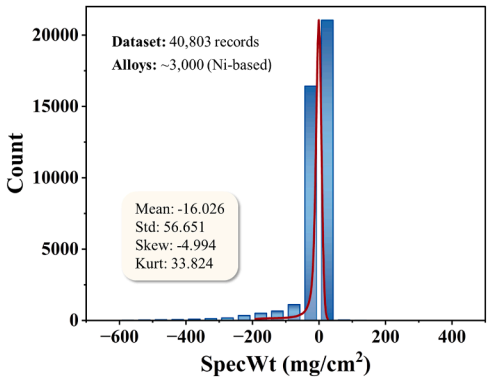

Fig. 2. Distribution of specific weight change (SpecWt) for Ni-based alloys under cyclic oxidation, with the red curve representing the Kernel Smooth fit.

To evaluate the dependency between the features and the target variable more comprehensively, particularly in capturing nonlinear relationships, a method of mutual information (MI) was introduced as an additional metric, due to its capability to capture both linear and nonlinear dependencies without assuming a specific functional form [33,34]. MI quantifies the statistical dependence between two random variables, and is defined as follows:

$$I(X;Y) = \sum_{x\in X}\sum_{y\in Y} p(x,y)\log\frac{p(x,y)}{p(x)p(y)} \tag{2}$$

where $p(x,y)$denotes the joint probability distribution of X and Y, while $p(x)$ and $p(y)$ are the marginal probability distributions.

Fig. 3c ranks the top 10 features by their MI scores with SpecWt. Consistent with the PCC analysis, Al and Cr related features rank highly, underscoring their dominant influence on protective scale formation. Crucially, the physics-informed descriptors ΔG_f and Val^{eff} also show high MI scores, validating the integration of thermodynamic and defect-chemistry features to capture fundamental drivers of alumina formation. Furthermore, notable MI scores for Ni and Cycle highlight the respective roles of matrix composition and cyclic thermal exposure in oxidation kinetics. This MI-based ranking thus complements linear analysis by revealing key nonlinear feature–target dependencies.

Features exhibiting MI scores below 0.05 were excluded as non-informative (see Supplementary Table S2 for all MI values). The removal of 17 elements (Cu, Th, Mn, V, N, O, La, Re, Pt, Ce, Misch, Sm, Er, Gd, Ga, Ru, Pd) through this screening produced a final dataset of 40,803 samples with 24 features.

Subsequent feature engineering was performed to identify and retain the most predictive feature subset. The dataset was randomly split into a 70% training set and a 30% test set. A Sequential Backward Elimination (SBE) procedure was employed, as illustrated in Fig. S2. Model performance was evaluated using the following three metrics: the coefficient of determination (R^2), mean absolute error (MAE), and root mean square error (RMSE), defined as follows:

$$R^2 = 1 - \frac{\sum_{i=1}^{n}(y_i - \hat{y}_i)^2}{\sum_{i=1}^{n}(y_i - \bar{y})^2} \tag{3}$$

$$MAE = \frac{1}{n}\sum_{i=1}^{n}|y_i - \hat{y}_i| \tag{4}$$

$$RMSE = \sqrt{\frac{1}{n}\sum_{i=1}^{n}(y_i - \hat{y}_i)^2} \tag{5}$$

where n is the number of samples, y_i and $\hat{y}_i$ represent the observed and predicted values of the i-th instance, respectively, and $\bar{y}$ denotes the mean of all observed values. R^2 serves as a metric to assess the goodness-of-fit of regression models, with a range from 0 to 1. High R^2 value

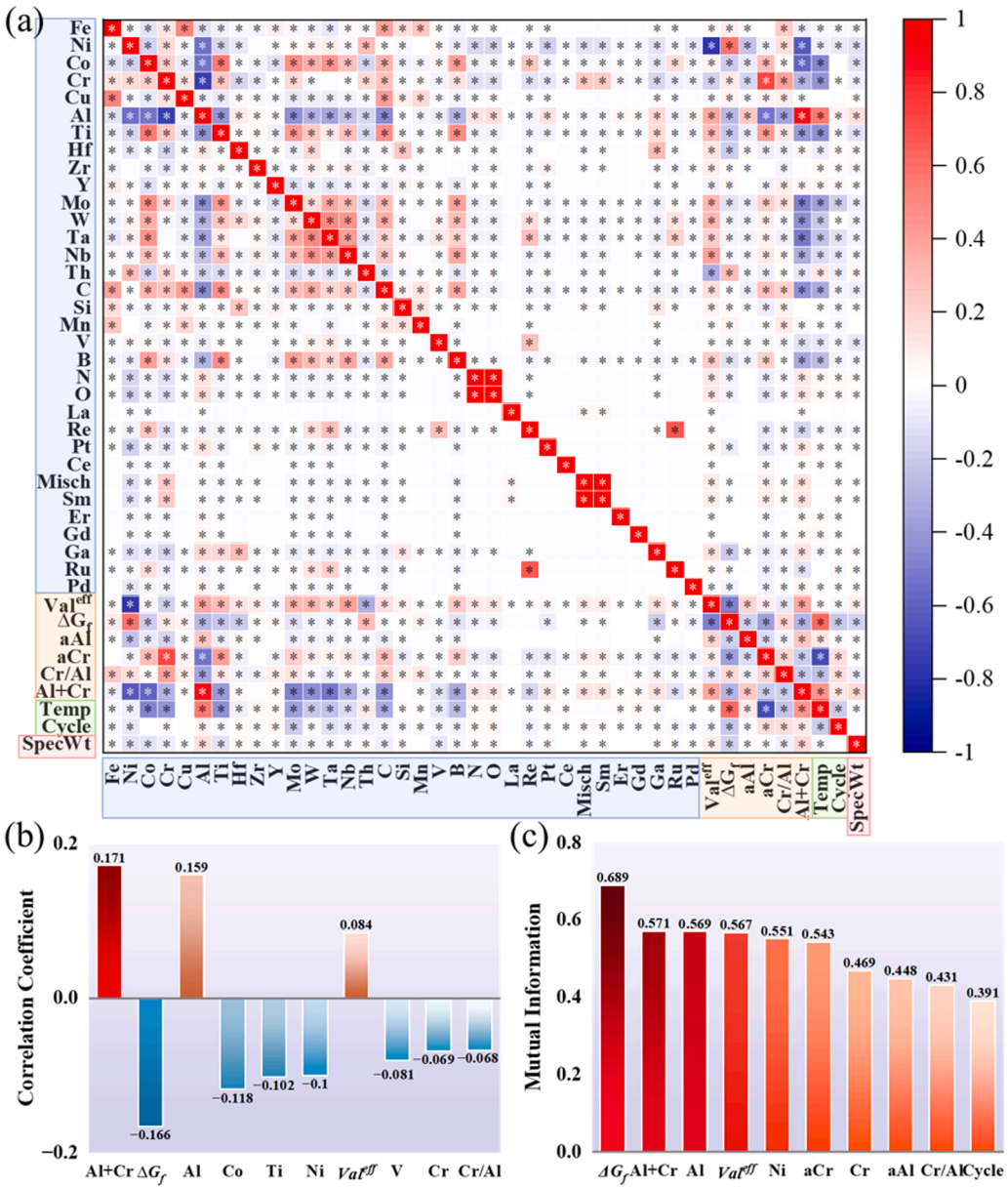

Fig. 3. Feature selection analysis: (a) Pearson correlation matrix, (b) top PCC-ranked features, and (c) top MI-ranked features for SpecWt prediction.

means a strong correlation between predictions and measurements, while lower MAE, RMSE values reflect higher predictive accuracy.

The optimal feature subset for a given algorithm was defined as the one that yielded the highest average R^2 score under 10-fold cross-validation on the training set. To avoid bias from any single model, this feature engineering process was repeated for each of the six regression algorithms considered in this study: XGBoost, LightGBM, CatBoost, Random Forest (RF), Multi-Layer Perceptron (MLP), and K-Nearest Neighbors (KNN). These algorithms were selected for their proven capability to handle nonlinear and skewed data, and their demonstrated effectiveness in materials property prediction. In addition, they were chosen as representative models from different regression families, including boosting-based, bagging-based, distance-based, and neural-network approaches, so as to provide a balanced comparison of commonly used machine-learning methods for nonlinear materials-property prediction.

3. Results and discussion

3.1. Comparative performance of machine learning algorithms

Fig. 4a-f presents the performance of the six candidate algorithms, with the primary criterion for comparison being their R^2 scores on the independent test set, which best reflects generalization performance, alongside their fitting accuracy on the training set. Each model was trained using its unique optimal feature subset, as identified during the feature engineering process and detailed in Supplementary Table S3.

Notably, for the present dataset, tree-based models demonstrated superior performance compared to other model types. This advantage is attributed to the inherent characteristics of tree-based algorithms, which excel at handling nonlinear relationships and skewed data distributions through hierarchical feature splitting [35–37]. Among the models, XGBoost exhibited an optimal balance between fitting accuracy and generalization ability, achieving an R^2 value of 0.891, an MAE of 7.068, and an RMSE of 16.868 on the training set. More importantly, on the independent testing set, the XGBoost model demonstrated strong

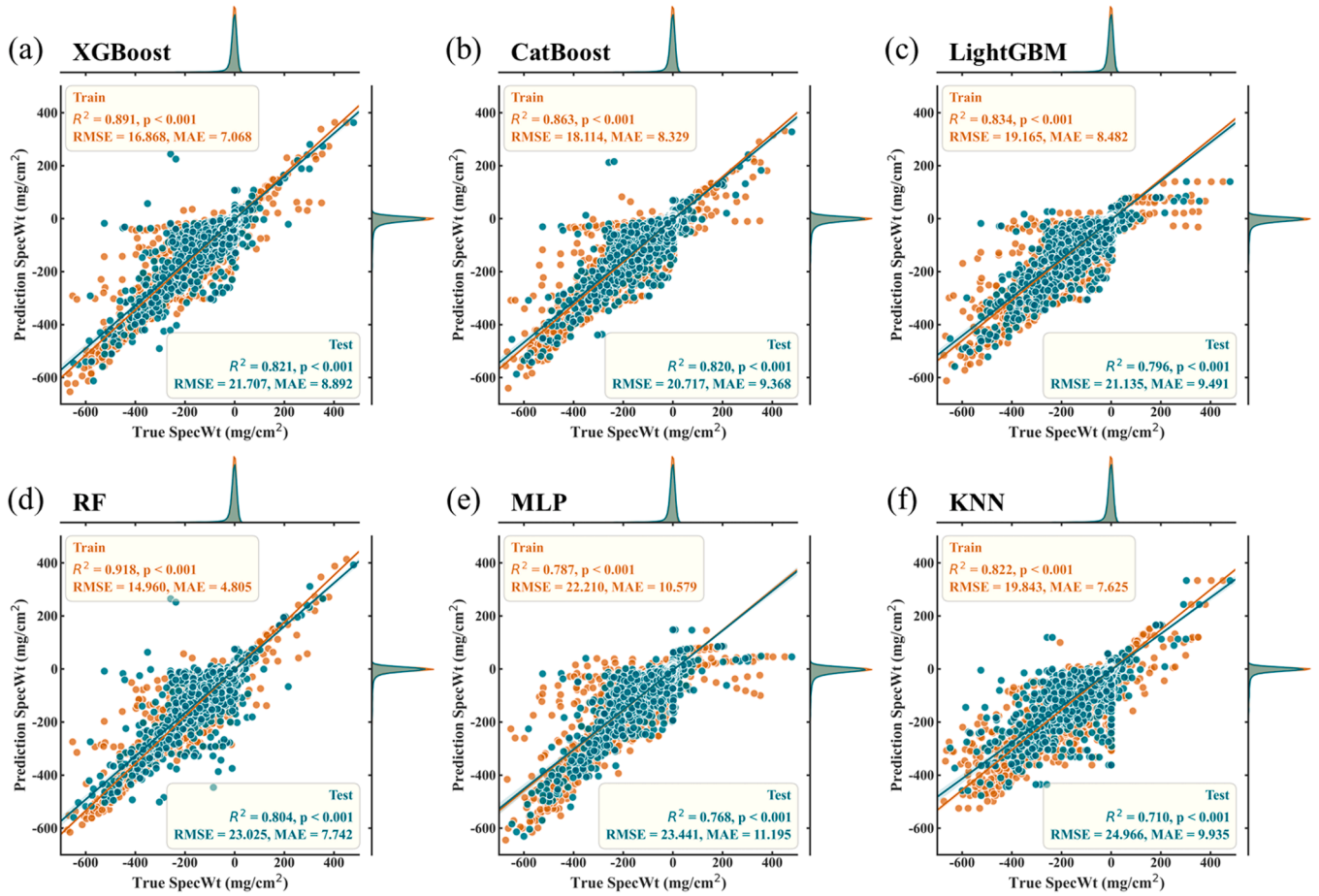

Fig. 4. Comparative performance evaluation of six regression algorithms using optimized feature subsets: (a) XGBoost, (b) CatBoost, (c) LightGBM, (d) RF, (e) MLP, and (f) KNN.

generalization to unseen data, with an R^2 value of 0.821, an MAE of 8.892, and an RMSE of 21.707. These results are comparable to those reported in prior machine learning studies on metal oxidation [27,28,38]. Based on its consistent robustness across both training and testing datasets, XGBoost was selected as the regression algorithm for subsequent analysis.

Subsequently, a Bayesian optimization framework coupled with 10-fold cross-validation was utilized to tune the hyperparameters of the XGBoost model. Bayesian optimization is a global optimization method based on probabilistic surrogate models, which efficiently explores the hyperparameter space by constructing Gaussian process estimates of the objective function. This approach leverages prior knowledge to guide the search direction, significantly reducing computational costs compared to traditional methods like grid search, especially in high-dimensional spaces. The search spaces for key hyperparameters (e.g., learning rate, maximum depth, and number of estimators) and the final

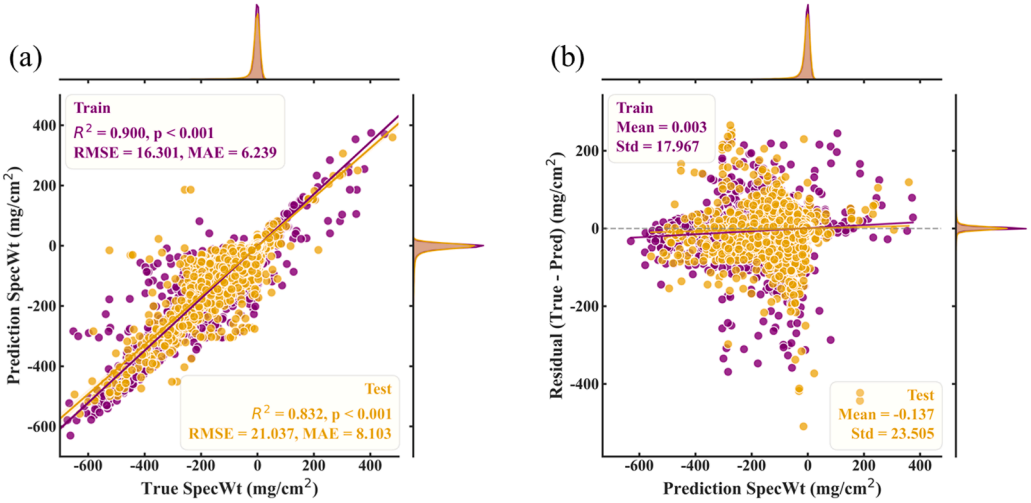

Fig. 5. Performance evaluation of the XGBoost_BO model: (a) predicted versus measured values scatter plot and (b) residual analysis plot.

optimized values are provided in Table S4.

Fig. 5 presents the performance evaluation of the hyperparameter-optimized XGBoost model (XGBoost-BO). The prediction scatter plot (Fig. 5a) shows that both training (purple circles) and test (yellow circles) data points form a dense cluster along their respective fitted regression lines, demonstrating a strong agreement between predictions and measured values. The accompanying marginal distributions indicate that the predicted and true values follow nearly identical patterns, further confirming the model's fidelity. Quantitatively, the model achieves a high R^2 of 0.900 (with RMSE = 16.301, MAE = 6.239) on the training set and 0.832 (with RMSE = 21.037, MAE = 8.103) on the test set, confirming excellent fitting performance and generalization capability. Furthermore, the residual plot (Fig. 5b) confirms the model's robustness, as residuals are randomly and symmetrically distributed around the zero line, with means of 0.003 (train) and −0.137 (test) and no observable systematic bias. These results collectively demonstrate the reliability of the XGBoost-BO model in predicting cyclic oxidation behavior, supporting its potential for practical application.

3.2. Predictive validation of cyclic oxidation kinetics

To validate the effectiveness of the constructed XGBoost-BO model in predicting oxidation kinetics, we applied it to six typical alloys (compositions listed in Table S6) reported in the literature [39–41], as shown in Fig. 6a. The model predicted the oxidation kinetics curves (SpecWt versus the number of cycles) for these alloys subjected to 200 thermal cycles at 1100 °C (Fig. 6b). The comparison reveals that the predicted cyclic oxidation curves overall agree well with the experimental results. The model accurately captures the primary weight change trends for different alloys and effectively distinguishes their relative cyclic oxidation resistance. The slight error between the predicted and experimental final SpecWt values after 200 cycles further confirms the model's satisfactory predictive accuracy and reliability.

A detailed quantitative assessment is provided by the scatter plot of predicted versus measured SpecWt values in Fig. 6c. The data points are categorized into two distinct regimes based on the number of cycles: the early oxidation stage (≤50 cycles, red points) and the later stage (>50 cycles, blue points). This 50-cycle cutoff is used for statistical robustness because the onset of quasi-linear mass change differs among alloys; a unified threshold retains sufficient early-stage points for fitting and reduces the impact of stochastic scatter on model assessment. The disparity in R^2 between these two regimes is pronounced. The early-stage data exhibits a low R^2 value of 0.240, indicating a weak correlation between predictions and measurements. In contrast, the later-stage data shows a high R^2 value of 0.880, demonstrating the model's strong predictive accuracy once the oxidation process stabilizes.

This dichotomy elucidates the model's performance across different phases of cyclic oxidation. The initial, transient oxidation phase is characterized by complex and stochastic processes such as the rapid formation of the initial oxide scale, the competition between metastable and stable oxides, and local spallation during the early thermal cycles. These phenomena are inherently difficult to predict with high precision, leading to the observed scatter in the early cycles. However, as the number of cycles increases, the oxidation process typically enters a steady-state regime dominated by the repeated growth and spallation of a stable, protective scale (e.g., Al_2O_3). The model excels in capturing the kinetics of this stabilized regime, as evidenced by the high R^2 value for the later cycles. The minor error between the predicted and experimental final SpecWt values after 200 cycles further confirms the model's satisfactory predictive accuracy and reliability for assessing long-term cyclic oxidation resistance.

3.3. Model interpretation via SHAP analysis

To elucidate the mechanisms behind the machine learning model's predictions of alloy performance in cyclic oxidation tests (quantified by the SpecWt metric), SHAP (SHapley Additive exPlanations) analysis was employed to interpret the XGBoost-BO model. This approach quantifies the global contribution of each input feature to the SpecWt target. The SHAP value indicates the direction and magnitude of a feature's influence on the prediction: a negative value corresponds to a decrease in SpecWt, implying degraded oxidation resistance, while a positive value signifies an increase in SpecWt, indicating improved performance. This analysis helps identify critical features and uncover their underlying relationships with cyclic oxidation behavior.

As shown in Fig. 7a, the mean absolute SHAP value indicates the importance of a feature on predicting SpecWt. Cycle ranks as the most influential feature, accounting for 22.3% of the total importance, followed by ΔG_f (17.3%), Al (10.6%), Al+Cr, Co, Temp, and others. The result demonstrates that the number of cycles (Cycle) is the most

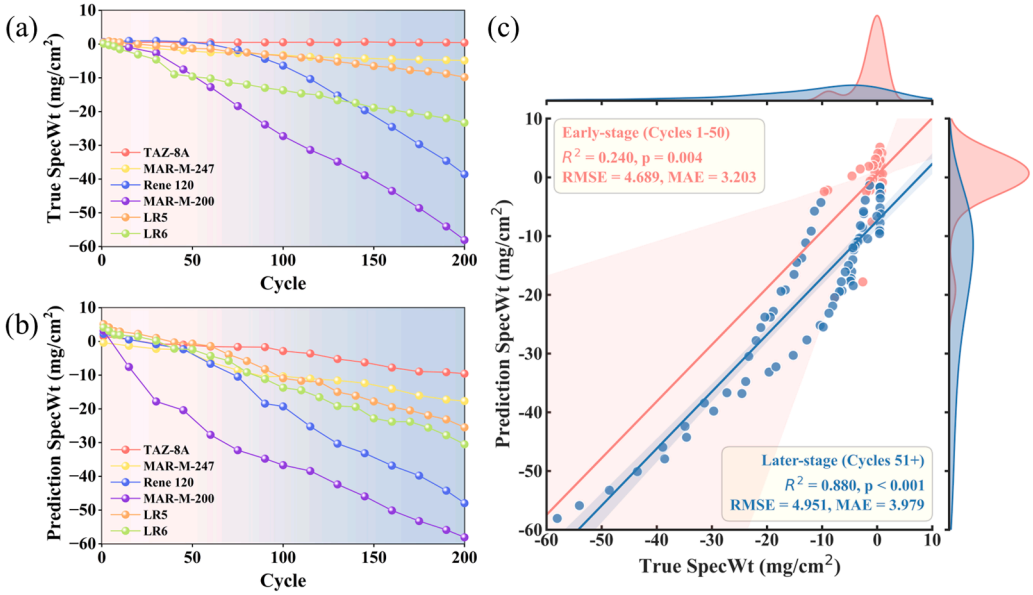

Fig. 6. Experimental validation of the XGBoost-BO model: Comparative analysis of (a) measured kinetics [39–41], (b) predicted kinetics, and (c) correlation between predicted and measured SpecWt categorized by early (≤50 cycles, red) and later (>50 cycles, blue) stages.

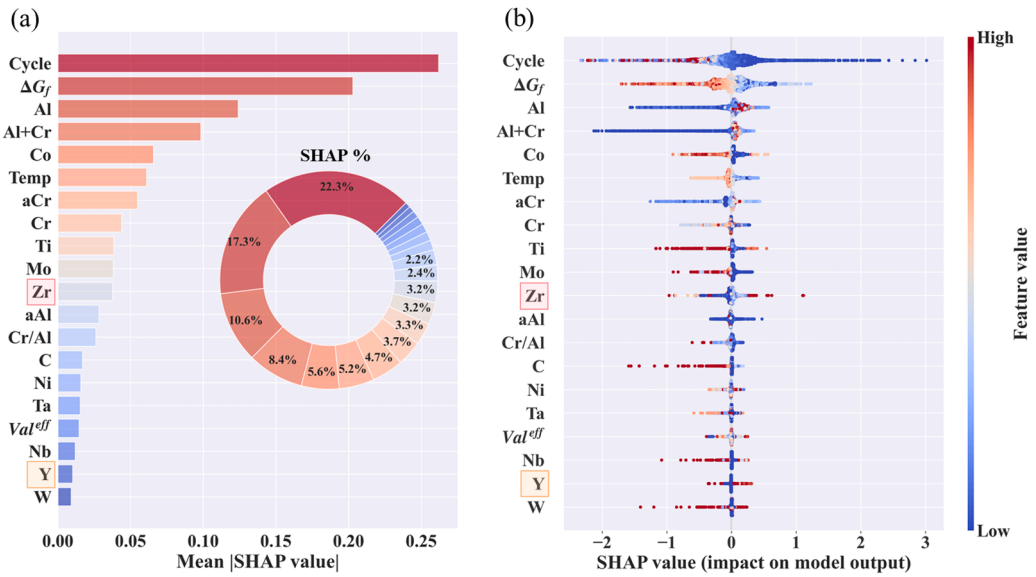

Fig. 7. SHAP analysis of the XGBoost-BO model: (a) feature importance ranking and (b) summary plot of feature impacts.

dominant factor influencing the weight loss, highlighting the cumulative damage inherent in cyclic oxidation. The formation free energy of Al_2O_3 (ΔG_f) and the aluminum content (Al) are also identified as key features. This strongly reflects the critical role of the protective Al_2O_3 scale in high-temperature oxidation resistance and signifies that its thermodynamic stability significantly influences the alloy's cyclic oxidation performance. To further explore mechanistic insights, the SHAP summary plot (Fig. 7b) visualizes the directionality of feature effects. Each point represents a sample, with the x-axis showing the SHAP value (approximately −2–3) and the y-axis listing all 20 input features. The color gradient from blue to red indicates the feature value from high to low. A clear negative correlation is observed for Cycle, as the SHAP value decreases with cycle number, demonstrating accelerated oxidation damage upon cycling. Temperature also shows a negative correlation, confirming that higher temperatures promote weight loss. The negative correlation for ΔG_f indicates that a more negative formation free energy favors the formation of a protective Al_2O_3 scale, thereby enhancing oxidation resistance. In contrast, Al content and the combined Al+Cr content exhibit positive correlations, supporting their protective roles: high Al content promotes a continuous Al_2O_3 layer, while the synergy between Al and Cr improves the scale's stability and adhesion. These observations align well with the established understanding of cyclic oxidation behavior in high-temperature alloys [42–44].

Notably, the influence of Cr exhibits marked nonlinearity. At low levels, Cr generally corresponds to positive SHAP values, suggesting a beneficial effect by promoting the formation of a protective Al_2O_3 scale. As the Cr content increases, however, the SHAP values turn negative. This is attributed to the formation of a Cr_2O_3-dominated scale at high Cr levels, which offers inferior cyclic oxidation resistance compared to Al_2O_3 [45]. This transition is also reflected in the Cr/Al ratio; when this ratio exceeds a certain threshold, the SHAP value shifts from positive to negative, indicating a detrimental effect. Interestingly, at very high Cr concentrations (represented by dark blue points in the plot), the SHAP values become positive again, which can be explained by the presence of Cr-rich alloys in the dataset where a protective Cr_2O_3 scale is effective, particularly at lower temperatures [46–48]. Furthermore, Cr activity shows a positive correlation with the SHAP value, implying that its thermodynamic activity exerts an influence on the oxidation mechanism independent of its concentration. In contrast, Al activity shows less correlation, because its importance is already captured by other Al-related parameters with high SHAP values.

Regarding other alloying elements, Co, Ti, and Mo generally exhibit negative correlations with the SHAP value, suggesting that excessive additions may adversely affect the oxide scale structure. A limited number of high-value samples display positive SHAP contributions, which likely reflects the breadth of alloy systems and test conditions encompassed in the database; nevertheless, the dominant trend remains negative. Elements such as C, Ta, Nb and W generally yield low SHAP values, implying their limited impact on SpecWt. Their influence is dualistic in nature; they may slightly improve performance at optimal levels but become detrimental beyond a certain threshold. This behavior reflects their complex role in modifying the composition and structure of the oxide scale. Ni, as a base matrix element, shows low influence on the SHAP value. More importantly, the descriptor Val^{eff} demonstrates weak correlation with SpecWt, plausibly because the dissolution and participation of alloying elements in the Al_2O_3 scale are non-proportional and system-dependent, which can obscure any simple relationship between effective valence metrics and cyclic oxidation behavior.

A notable observation concerns the rare-element descriptors: the model assigns a substantially higher importance to Zr than to Y, which is not fully consistent with some experimental narratives emphasizing strong “reactive-element” effects of Y [49–52]. This discrepancy may be influenced by dataset imbalance, since Zr-containing alloys account for 58.9% of the database whereas Y-containing alloys represent only 9%, which can reduce the statistical salience of Y during training and thus depress its global SHAP importance. The single-element SHAP dependence plots (Supplementary Fig. S3) further indicate that Y additions are predominantly beneficial at low contents (most data points at <1 wt% show positive SHAP values), but the effect becomes mixed near ~1 wt%, where approximately half the points exhibit negative SHAP values—suggesting that excessive Y may promote oxide formation and accelerate degradation under certain conditions [53]. Notably, the SHAP response peaks around ~0.4 wt% Y, implying a potential optimal doping window. Zr shows a similarly positive overall tendency, yet exhibits a pronounced positive SHAP response around ~1.4 wt%, consistent with both its higher model-attributed relevance and a stronger stabilizing effect on the protective scale. Mechanistically, this can be rationalized by the stronger metal-oxygen bonding: Zr-O bond strength is substantially higher than Al-O and slightly higher than Y-O, which can more effectively impede transport and reduce the growth rate of alumina, thereby enhancing scale stability and improving cyclic oxidation resistance [54].

To address the effect of data imbalance, we fixed the Y-containing alloys a weight of 6.5 (matching the Zr/Y ratio of 58.9%/9.0%) during

XGBoost-BO training, while keeping other samples at unit weight. The re-weighted model still performed well (test R^2 = 0.830, MAE = 7.58, RMSE = 23.57). As shown in Fig. 8, the SHAP importance of Y rose significantly (up seven ranks), but remained four ranks below Zr. This evolution illustrated that the imbalance to some extent but not fully explains the Zr-Y difference. Zr's importance also increased moderately, suggesting the weighting boosts sensitivity to reactive elements in general, not just Y. Notably, the top factors (Cycle, ΔG_f, Al, Al+Cr) stayed unchanged, confirming the model's main mechanistic conclusions are robust.

3.4. Composition-oxidation relationships in Ni-Cr-Al system

To gain deeper insight into the Ni-Cr-Al system, the ML model was employed to predict the SpecWt changes across comprehensive composition ranges of 0–45 at% for Al and 0–45 at% for Cr, with Ni serving as the balance. As the fundamental basis for the majority of nickel-based superalloys, the oxidation behavior of this system is well-established. Comparing the model predictions with classical knowledge allows a direct assessment of whether the model captures the fundamental physical principles governing composition-oxidation performance relationships, thereby enhancing the model's interpretability and reliability.

Extensive experimental studies have shown that Ni-Cr-Al ternary alloys can form three main types of oxide scales under high-temperature oxidation conditions—NiO, Cr_2O_3, and Al_2O_3—as illustrated in Fig. 9a. The type of oxide scale formed is governed by the total Cr + Al content and the Cr/Al ratio. When the Cr + Al content is insufficient (e.g., less than 11 wt% [15]), NiO forms, offering minimal oxidation protection. When the Cr + Al content is sufficient but Cr predominates (e.g., the Cr/Al ratio exceeds a critical threshold of 2.11 [15]), a Cr_2O_3 scale forms, which provides moderate high-temperature resistance. In contrast, when the Cr/Al ratio falls below this threshold and Al predominates, a protective Al_2O_3 scale develops, yielding optimal oxidation resistance. Fig. 9a also presents the SpecWt values predicted by the ML model for the Ni-Cr-Al ternary system, which align well with the experimentally established oxide-scale formation boundaries [15,16]. This agreement indicates that the model accurately correlates alloy composition with SpecWt and offers insight into the likely type of oxide scale formed.

The SHAP dependence plot for Al+Cr (Fig. 9b) shows that SHAP values become positive when Al+Cr exceeds 20 at%, consistent with the crucial role of both elements in forming a protective Al_2O_3 scale, as noted earlier. The SHAP plot for Cr/Al (Fig. 9c) reveals positive SHAP values when Cr/Al is below 0.9, highlighting the beneficial effect of minor Cr additions in promoting the early formation of an Al_2O_3 scale through the well-known "third-element effect" [55–58]. However, for Cr/Al ratios above 0.9, most data points correspond to negative SHAP values, suggesting that excessively high Cr/Al ratios may hinder alumina formation and adversely affect oxidation resistance. This underscores the importance of maintaining an optimal Cr/Al ratio to ensure the effective development of a continuous Al_2O_3 scale.

3.5. Screening for oxidation-resistant compositions

Leveraging the well-trained XGBoost-BO model, this study systematically explored the vast composition space of nickel-based superalloys to design compositions with superior cyclic oxidation resistance. To focus on the effects of core alloying elements, only the contents of eight elements—Ni, Co, Cr, Al, Ti, Mo, W, and Ta—were considered. The model output was the SpecWt after 200 thermal cycles at 1100 °C, which directly characterizes the alloy's cyclic oxidation resistance. To improve the reliability of extrapolative predictions through this virtual design space, an ensemble of independently trained XGBoost-BO models was employed. For each virtual composition, the final predicted performance was selected as the ensemble mean predicted SpecWt, while the prediction confidence was quantified by the standard deviation of the ensemble predictions. The composition ranges for these elements were set as shown in Table 2, covering ranges typical for superalloy design. A grid sampling with a 1% step size within this 8-dimensional composition space generated 817,306 unique virtual alloy compositions for prediction. For the high-throughput screening of virtual compositions, a_{Al} and a_{Cr} were accessed by a surrogate model of Bayesian-optimized XGBoost based on the original thermodynamic dataset. This dataset was calculated with the Thermo-Calc 2025 A software and TCNi12 database. The other thermodynamic descriptors were subsequently derived from the predicted activities and alloy compositions according to the equations listed in Table 1, where the complete descriptor set was then used for SpecWt prediction (more details provided in Supplementary Fig. S5).

To reveal the underlying relationships between composition and performance in the high-dimensional data, Uniform Manifold Approximation and Projection (UMAP) was utilized for dimensionality reduction and visualization of the prediction results (Fig. 10). UMAP effectively preserves the local structure of data points from the high-

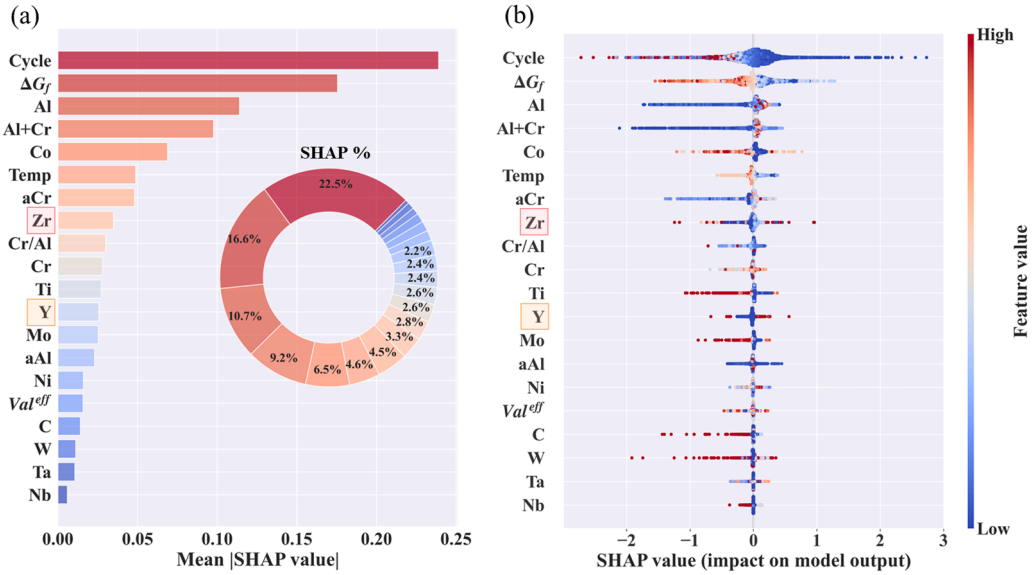

Fig. 8. SHAP analysis of the re-weighted XGBoost-BO model: (a) feature importance ranking and (b) summary plot of feature impacts.

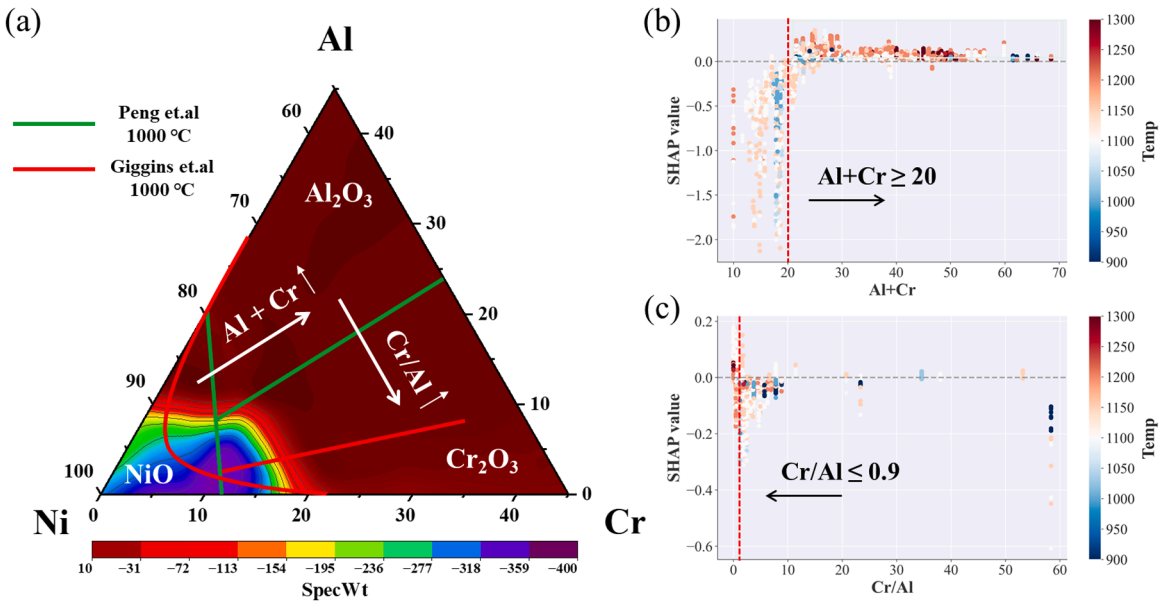

Fig. 9. Decoding composition-oxidation relationships in the Ni-Cr-Al system: (a) Model-predicted SpecWt overlaid on the experimental oxide-formation regime diagram [15,16]. (b) SHAP dependence of SpecWt on Al+Cr content, and (c) on Cr/Al ratio.

Table 2
Chemical composition space defined for the prediction of cyclic performance (Ni is in balance).

Content (at%)	Ni	Al	Cr	Co	Ti	Mo	W	Ta
Minimum	60	8	6	0	0	0	0	0
Maximum	80	15	15	10	5	5	5	5

dimensional space on a 2D plane, intuitively showing the clustering trends of alloys with similar compositions in terms of performance [59,60]. The results show that the distribution of SpecWt (color gradient) correlates strongly with regions corresponding to specific elements, reflecting the element-property relationships captured by the ML model. The close match between the measured results (marked data points, their compositions provided in Table S5) and predictions further validates the model's robustness and predictive accuracy. A close correspondence is also observed between the spatial distributions in Fig. 10a and Fig. 10b, indicating that regions with the more negative values of calculated SpecWt generally exhibit the higher predictive uncertainty. This suggests that the most unfavorable predicted regions are also associated with lower prediction confidence.

The mean-prediction map reveals a strong spatial correlation between higher SpecWt values and regions of high aluminum content, underscoring the decisive role of Al in forming a protective Al_2O_3 scale. In contrast, lower SpecWt values are predicted in compositions rich in Cr but deficient in Al. At 1100 °C, Cr struggles to form a stable oxide scale, as Cr_2O_3 may further oxidize to volatile species such as CrO_3 or $CrO_2(OH)_2$, leading to scale failure and increased mass loss [7,61,62]. This volatility is exacerbated in rapidly moving gas streams, fundamentally limiting the protective capability of chromia-forming alloys at such elevated temperatures. Consequently, oxidation resistance under these conditions depends primarily on the formation of a continuous Al_2O_3 layer. The most severe degradation, corresponding to the lowest SpecWt values, occurs in high-Ni regions with insufficient Cr and Al, where a non-protective NiO scale forms. This oxide grows rapidly, resulting in a friable structure with prevalent voids and microcracking that promotes spallation and sustained attack [1,63,64]. Meanwhile, the spatial distributions of Co, Ti, Mo, W, and Ta show little overlap with the SpecWt pattern, suggesting their secondary influence on cyclic oxidation performance within this system at 1100 °C.

Following the initial prediction across the vast composition space, constraints were applied based on SHAP dependence plots to screen for Ni-based superalloy compositions with superior cyclic oxidation resistance. These plots reveal the non-linear relationships between element content and the SpecWt target, providing a quantitative basis for compositional screening. To characterize the complex variation of elemental contributions to SpecWt, SHAP values were analyzed using a Generalized Additive Model (GAM) [65,66]. The results for three key elements (Al, Cr, Co) are presented in Fig. 11c-e, with the remainder in Supplementary Fig. S4. The GAM fitting confirmed distinctly non-linear influences. Al and Co exhibited generally monotonic trends, whereas Cr showed more complex behavior, with SHAP values near zero or positive only below ~8 at%. A conservative screening strategy was therefore implemented, incorporating intervals with positive or near-zero SHAP values. Given that Ni's SHAP values consistently fluctuated near zero and its role as a matrix element, it was left unconstrained. The final constraints (Table 3), including the total (Al+Cr) limit from Section 3.4, defined the promising elemental ranges for achieving high cyclic oxidation resistance.

Under the GAM-SHAP constraints, the retained virtual compositions cluster within high-performance regions of the UMAP space (Fig. 11a). To avoid selecting unreliable candidates from underexplored areas, an uncertainty-based filter was added after the GAM-SHAP step. This uncertainty metric showed a strong positive correlation with absolute prediction error on the test set (Supplementary Fig. S6). Thus, only compositions with predictive uncertainty below 4.03 (the 80th percentile of test-set uncertainty; Supplementary Table S6) were kept, as shown in Fig. 11b. This approach ensures that the final selections are supported by favorable compositional windows, high predicted SpecWt, and high predictive confidence.

To further test the model's reliability, two single-crystal Ni-based alloys (NS1 and NS2) were prepared for comparison. The related compositions (Table 4) lay within the final uncertainty-filtered window (Fig. 11b). Cyclic oxidation tests were performed at 1100 °C for 200 cycles, with three repetitions per alloy to improve the accuracy. Each cycle consisted of three stages: heating to 1100 °C, holding for 1 h, and then cooling in air. The specific weight change was measured during the tests. The ensemble XGBoost-BO model was employed to predict the oxidation kinetics of NS1 and NS2 under the same thermal cycling conditions.

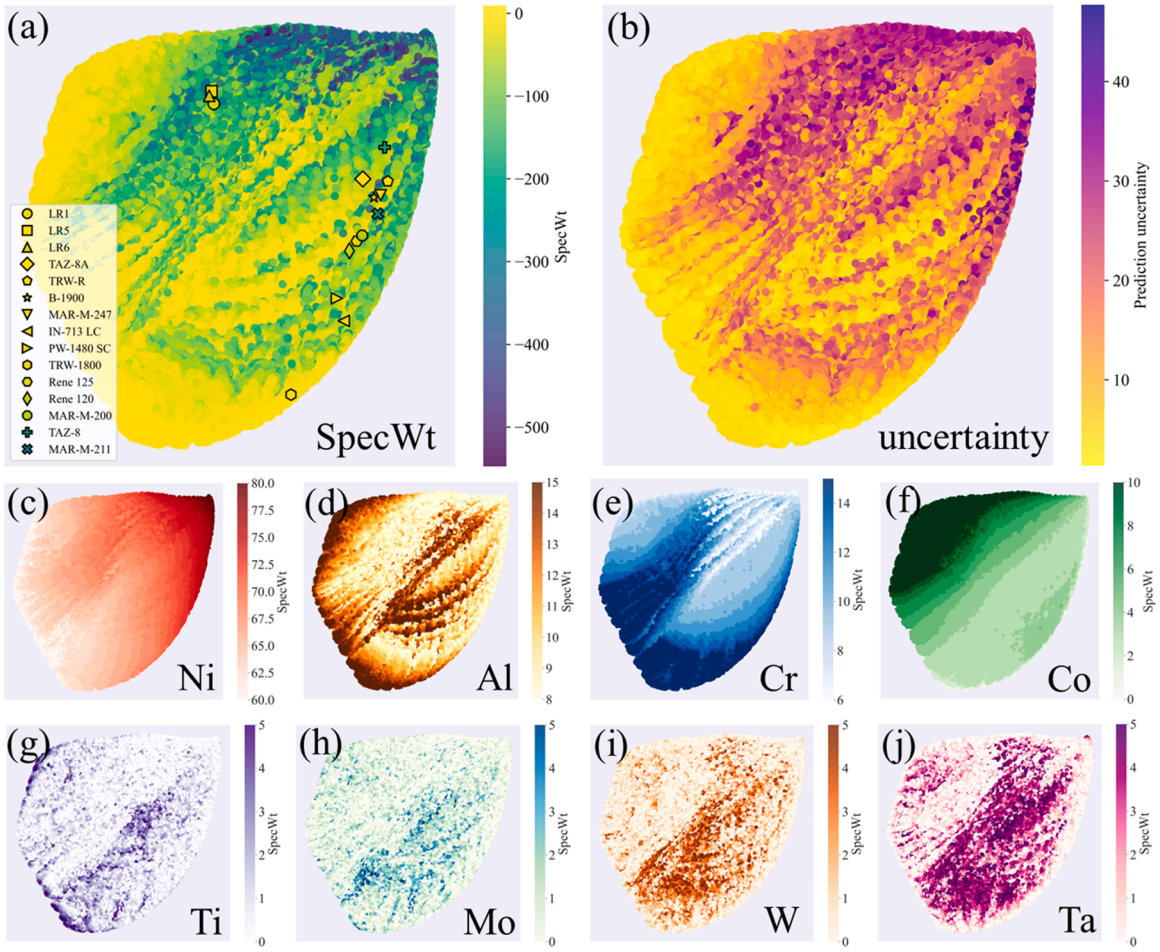

Fig. 10. UMAP visualization of the composition-performance relationship for Ni-based superalloys. (a) UMAP projection colored by the mean predicted SpecWt values, with overlaid experimental data points for 15 independent alloys (compositions in Table S6). (b) Corresponding predictive uncertainty quantified as the standard deviation of ensemble predictions. (c-j) Distribution of elemental compositions for (c) Ni, (d) Al, (e) Cr, (f) Co, (g) Ti, (h) Mo, (i) W, and (j) Ta across the UMAP space.

Fig. 12 compares experiment and prediction indicating that both NS1 and NS2 behavior good cyclic oxidation performance. The measured SpecWt values are slightly higher than predicted, indicating slightly better performance than the model expected. However, the predicted and measured kinetics follow the same overall trends, including a similar transition from an initial parabolic regime to a steeper quasi-linear regime at later cycles. The experimental error bars and predictive uncertainty bands partially overlap at all measured cycle numbers, so the differences are acceptable. Notably, the model shows less variation and lower uncertainty at the very early stage, but the uncertainty band becomes wider later, suggesting the model is more reliable during the stabilized oxidation stage. Post-oxidation XRD and cross-sectional SEM/EDS results for both alloys after 200 cycles are given in Supplementary Figs. S7 and S8.

This section demonstrates a data-driven methodology for screening key elemental ranges that promote exceptional cyclic oxidation resistance in Ni-based superalloys and identifies favorable compositional windows, providing valuable guidance for the development of advanced oxidation-resistant high-temperature alloys. The experimental validation on NS1 and NS2 further shows that the model-guided screening strategy can be translated into physically measurable oxidation performance under representative cyclic-oxidation conditions. By integrating uncertainty-aware filtering with experimental verification, the final candidate selection is constrained not only by favorable compositional features but also by predictive reliability and practical relevance. Future efforts will focus on more precise composition optimization within the identified promising windows, supported by expanded high-quality datasets with more accurately measured minor-element contents and cyclic-oxidation kinetics.

4. Conclusions

A thermodynamic-informed ML framework was established to elucidate the cyclic oxidation performance of nickel-based alloys. The following conclusions were drawn:

(1) The established XGBoost model, optimized through feature engineering and Bayesian methods, achieved high accuracy (test set $R^2 > 0.83$) and generalizability in predicting SpecWt. It effectively captured complex relationships among composition, temperature, cycle number, and oxidation response, providing a reliable computational tool for cyclic oxidation assessment.
(2) SHAP analysis identified the number of cycles as the most significant factor for cumulative damage. Cyclic oxidation resistance is primarily governed by the thermodynamic driving force for Al_2O_3 formation (ΔG_f), realized through sufficient Al content and its synergistic effect with Cr. Critical compositional thresholds were identified, indicating that excessive Cr/Al ratios or over-additions of elements like Co, Ti, and Mo impaired protective scale formation.
(3) Validation on the Ni-Cr-Al ternary system confirmed the model's ability to accurately capture established composition-oxidation

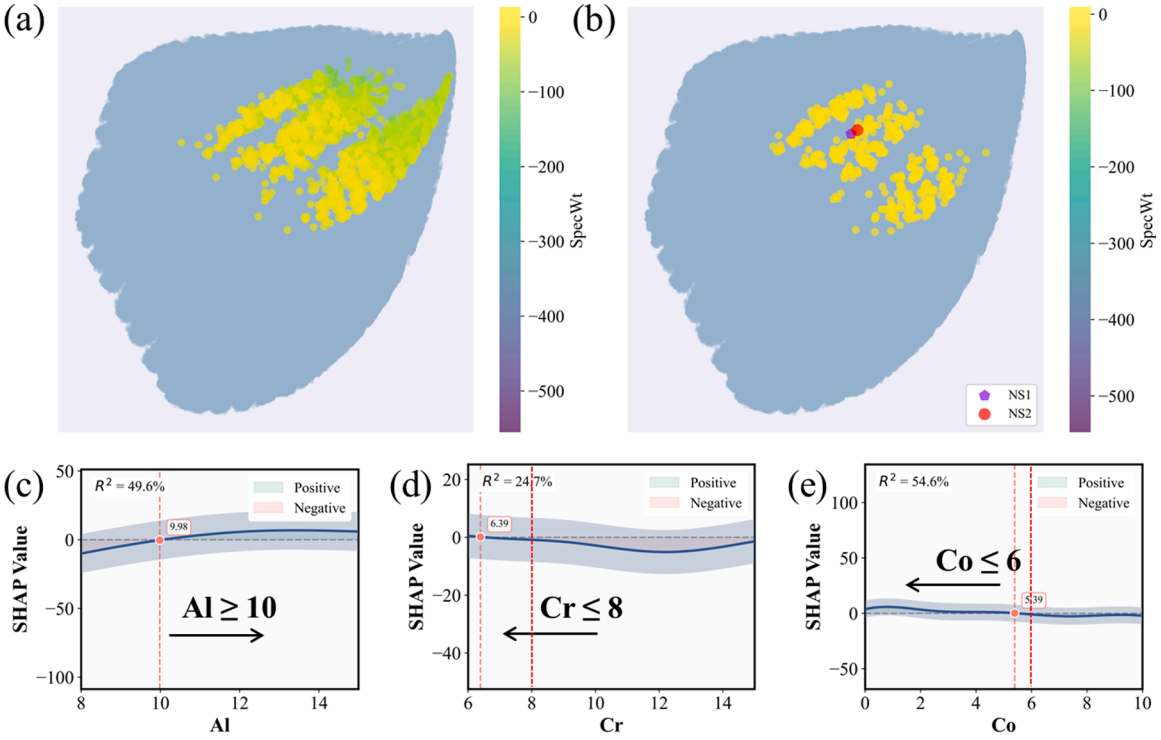

Fig. 11. Alloy screening based on GAM-fitted SHAP analysis and uncertainty-aware filtering. (a) UMAP projection of the GAM-SHAP-screened compositions, colored by the mean predicted SpecWt. (b) Corresponding high-confidence subset retained after applying the uncertainty constraint ($\sigma \leq 4.03$), where the experimentally validated alloys are highlighted by distinct marker shapes. (c-e) SHAP dependence plots for (c) Al, (d) Cr, and (e) Co, with fits from the Generalized Additive Model (GAM). Red dashed lines and arrows indicate the critical thresholds and trends used for screening.

Table 3
Composition constraints for screening oxidation-resistant alloys derived from GAM-SHAP analysis.

Content (at%)	Ni	Al	Cr	Co	Ti	Mo	W	Ta	Al+Cr
Minimum	60	10	6	0	0	0	0	1	20
Maximum	80	15	8	6	1.5	2.5	3.5	2.5	23

Table 4
Chemical compositions (at%) of the newly designed single-crystal Ni-based superalloys (NS1 and NS2), measured by EPMA.

Alloy	Ni	Al	Cr	Co	Ti	Mo	W	Ta
NS1	Bal.	14.08	6.88	5.44	0.63	1.80	1.33	2.46
NS2	Bal.	14.00	6.58	5.40	0.65	1.02	2.05	2.43

relationships. The predicted SpecWt values aligned with experimental oxide-scale boundaries, demonstrating physical relevance in protective Al_2O_3 regimes.

(4) A model-guided screening strategy integrating compositional constraints and uncertainty-aware filtering was established for identifying promising Ni-based alloys, and its effectiveness was supported by experimental validation. Future efforts will emphasize closing the loop between data-driven screening, mechanism-informed alloy optimization, and broader validation under representative cyclic-oxidation conditions.

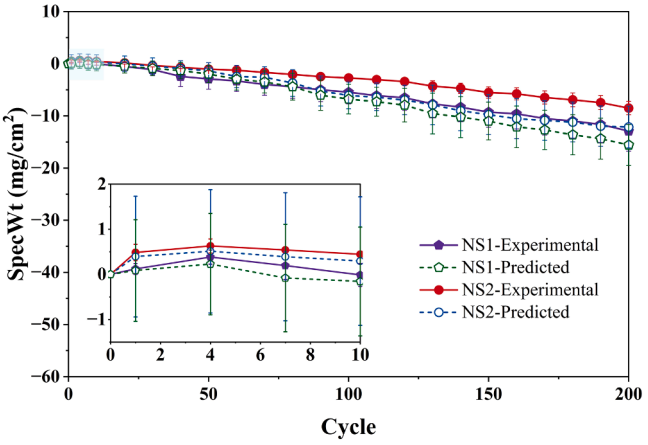

Fig. 12. Experimental validation of the screened alloys NS1 and NS2 under cyclic oxidation at 1100 °C for 200 cycles. The comparison was illustrated between the experimentally measured SpecWt values and the predictions based on ensemble XGBoost-BO, with error bars representing the standard deviation of three repeated experiments and the predictive uncertainty of the ensemble model, respectively.

CRediT authorship contribution statement

Liang Jiang: Software, Resources. **Aiying Wang:** Writing – review & editing, Validation, Supervision, Resources, Methodology, Funding acquisition, Conceptualization. **Xin Yu:** Software, Resources. **Xiaoyu Sun:** Writing – review & editing, Validation, Supervision, Resources, Methodology, Funding acquisition, Conceptualization. **Haoyi Xu:** Writing – review & editing, Writing – original draft, Methodology, Investigation, Data curation, Conceptualization. **Zhenyu Wang:** Writing – review & editing, Validation, Supervision, Funding acquisition. **Guanshui Ma:** Writing – review & editing, Validation, Supervision.

Declaration of Competing Interest

The authors declare that they have no known competing financial interests or personal relationships that could have appeared to influence

the work reported in this paper.

Acknowledgements

This research was supported by the National Key R&D Program of China (2024YFB3816500), National Natural Science Foundation of China (52501032, U22A20111), the Zhejiang Provincial Natural Science Foundation (LQ24E010005), and the Key R&D Program of Ningbo (2024Z096).

Appendix A. Supporting information

Supplementary data associated with this article can be found in the online version at doi:10.1016/j.corsci.2026.113909.

Data availability

The authors do not have permission to share data.

References

[1] R.C. Reed, The Superalloys Fundamentals and Applications, Cambridge University Press, Cambridge, 2006, https://doi.org/10.1017/CBO9780511541285.
[2] C.T. Sims, N.S. Stoloff, W.C. Hagel. Superalloys II, Wiley, New York, 1987.
[3] T.M. Pollock, Alloy design for aircraft engines, Nat. Mater. 15 (2016) 809–815, https://doi.org/10.1038/nmat4709.
[4] B. Yin, W. Yong, J. Zhu, H. Ge, S. Zhu, Y. Gui, W. Zhang, H. Fu, J. Xie, Compositional design of Ni-based superalloys for additive manufacturing: progress and perspectives, Mater. Sci. Eng. R. Rep. 169 (2026) 101185, https://doi.org/10.1016/j.mser.2026.101185.
[5] S. Cruchley, M.P. Taylor, R. Ding, H.E. Evans, D.J. Child, M.C. Hardy, Comparison of chromia growth kinetics in a Ni-based superalloy, with and without shot-peening, Corros. Sci. 100 (2015) 242–252, https://doi.org/10.1016/j.corsci.2015.07.033.
[6] R. Prescott, M.J. Graham, The formation of aluminum oxide scales on high-temperature alloys, Oxid. Met. 38 (1992) 233–254, https://doi.org/10.1007/BF00666913.
[7] N. Birks, G.H. Meier, F.S. Pettit, Introduction to the High Temperature Oxidation of Metals, Cambridge University Press, Cambridge, 2006, https://doi.org/10.2277/0521480426.
[8] C. Wagner, The theory of the warm-up process, Z. Phys. Chem. 21B (1933) 25–41.
[9] C. Wagner, Passivity and inhibition during the oxidation of metals at elevated temperatures, Corros. Sci. 5 (1965) 751–764, https://doi.org/10.1016/S0010-938X(65)80003-8.
[10] C. Wagner, Oxidation of alloys involving noble metals, J. Electrochem. Soc. 103 (1956) 571–581, https://doi.org/10.1149/1.2430159.
[11] G.R. Wallwork, The oxidation of alloys, Rep. Prog. Phys. 39 (1976) 401–485, https://doi.org/10.1088/0034-4885/39/5/001.
[12] A.U. Seybolt, Oxidation of metals, Adv. Phys. 12 (1963) 1–43, https://doi.org/10.1080/00018736300101253.
[13] R.L. Levin, J.B. Wagner, The role of a displacement reaction in the kinetics of oxidation of alloys, J. Electrochem. Soc. 108 (1961) 954–960, https://doi.org/10.1149/1.2427927.
[14] J. Benard, The oxidation of metals and alloys, Metall. Rev. 9 (1964) 473–503, https://doi.org/10.1179/mtlr.1964.9.1.473.
[15] X. Peng, H. Zhen, L. Tian, X. Wang, K. Wang, Y. Xie, A novel strategy to apply metallic nanoparticles to manufacture NiCrAl composite coatings smartly growing chromia and alumina, Compos. Part B Eng. 234 (2022) 109721, https://doi.org/10.1016/j.compositesb.2022.109721.
[16] C.S. Giggins, F.S. Pettit, Oxidation of Ni-Cr-AI alloys between 1000° and 1200 °C, J. Electrochem. Soc. 118 (1971) 1782.
[17] H.-S. Kim, S.-J. Park, S.-M. Seo, Y.-S. Yoo, H.-W. Jeong, H. Jang, Regression analysis of high-temperature oxidation of Ni-based superalloys using artificial neural network, Corros. Sci. 180 (2021) 109207, https://doi.org/10.1016/j.corsci.2020.109207.
[18] G. Sun, L. Jia, Z. Hong, G. Liu, H. Zhang, Improvement of oxidation resistance of Nb–Ti–Si based alloys with additions of Al, Cr and B at different temperatures, Prog. Nat. Sci. Mater. Int. 31 (2021) 442–453, https://doi.org/10.1016/j.pnsc.2021.04.006.
[19] H. Xu, X. Sun, R.L. Peng, J. Moverare, X.-H. Li, G. Ma, Z. Wang, A. Wang, Machine learning enabled the prediction of γ′-depleted depth during interdiffusion of bond-coated IN792 superalloy, Surf. Coat. Technol. 513 (2025) 132448, https://doi.org/10.1016/j.surfcoat.2025.132448.
[20] S.K. Dewangan, V. Kumar, Application of artificial neural network for prediction of high temperature oxidation behavior of $AlCrFeMnNiW_x$ (X = 0, 0.05, 0.1, 0.5) high entropy alloys, Int. J. Refract. Met. Hard Mater. 103 (2022) 105777, https://doi.org/10.1016/j.ijrmhm.2022.105777.
[21] D.W. Yun, S.M. Seo, H.W. Jeong, Y.S. Yoo, Effect of refractory elements and Al on the high temperature oxidation of Ni-base superalloys and modelling of their oxidation resistance, J. Alloy. Compd. 710 (2017) 8–19, https://doi.org/10.1016/j.jallcom.2017.03.179.
[22] Q. Wei, B. Cao, L. Deng, A. Sun, Z. Dong, T.-Y. Zhang, Discovering a formula for the high temperature oxidation behavior of FeCrAlCoNi based high entropy alloys by domain knowledge-guided machine learning, J. Mater. Sci. Technol. 149 (2023) 237–246, https://doi.org/10.1016/j.jmst.2022.11.040.
[23] D.W. Yun, S.M. Seo, H.W. Jeong, I.S. Kim, Y.S. Yoo, Modelling high temperature oxidation behaviour of Ni-Cr-W-Mo alloys with bayesian neural network, J. Alloy. Compd. 587 (2014) 105–112, https://doi.org/10.1016/j.jallcom.2013.10.138.
[24] C. Pei, Q. Ma, J. Zhang, L. Yu, H. Li, Q. Gao, J. Xiong, A novel model to predict oxidation behavior of superalloys based on machine learning, J. Mater. Sci. Technol. 235 (2025) 232–243, https://doi.org/10.1016/j.jmst.2025.01.071.
[25] G. Bianco, A. Nisar, C. Zhang, B. Boesl, A. Agarwal, Predicting oxidation damage in ultra high-temperature borides: a machine learning approach, Ceram. Int. 48 (2022) 29763–29769, https://doi.org/10.1016/j.ceramint.2022.06.236.
[26] S. Aghaeian, F. Nourouzi, W.G. Sloof, J.M.C. Mol, A.J. Böttger, Predicting the parabolic growth rate constant for high-temperature oxidation of steels using machine learning models, Corros. Sci. 221 (2023) 111309, https://doi.org/10.1016/j.corsci.2023.111309.
[27] C. Li, K. Xu, M. Lou, L. Wang, K. Chang, Machine learning-enabled prediction of high-temperature oxidation resistance for Ni-based alloys, Corros. Sci. 234 (2024) 112152, https://doi.org/10.1016/j.corsci.2024.112152.
[28] X. Tan, W. Trehern, A. Sundar, Y. Wang, S. San, T. Lu, F. Zhou, T. Sun, Y. Zhang, Y. Wen, Z. Liu, M. Gao, S. Hu, Machine learning and high-throughput computational guided development of high temperature oxidation-resisting Ni-Co-Cr-Al-Fe based high-entropy alloys, Npj Comput. Mater. 11 (2025) 93, https://doi.org/10.1038/s41524-025-01568-8.
[29] C.A. Barrett, A High Temperature Cyclic Oxidation Data Base for Selected Materials Tested at NASA Glenn Research Center (NASA/TM-2003-212546), NASA Glenn Research Center, 2003. ⟨https://ntrs.nasa.gov/citations/20030093726⟩.
[30] A. Sato, Y.-L. Chiu, R.C. Reed, Oxidation of nickel-based single-crystal superalloys for industrial gas turbine applications, Acta Mater. 59 (2011) 225–240, https://doi.org/10.1016/j.actamat.2010.09.027.
[31] J. Zhang, B. Xu, Y. Xiong, S. Ma, Z. Wang, Z. Wu, S. Zhao, Design high-entropy carbide ceramics from machine learning, Npj Comput. Mater. 8 (2022) 5–17, https://doi.org/10.1038/s41524-021-00678-3.
[32] J. Chen, W. Xu, R. Zhang, Δ-machine learning-driven discovery of double hybrid organic–inorganic perovskites, J. Mater. Chem. A 10 (2022) 1402–1413, https://doi.org/10.1039/D1TA09911F.
[33] B.-S. Oh, L. Sun, C.S. Ahn, Y.K. Yeo, Y. Yang, N. Liu, Z. Lin, Extreme learning machine based mutual information estimation with application to time-series change-points detection, Neurocomputing 261 (2017) 204–216, https://doi.org/10.1016/j.neucom.2015.11.138.
[34] J. Chen, F. Fan, C. Wei, K. Polat, F. Alenezi, Decoding driving states based on normalized mutual information features and hyperparameter self-optimized gaussian kernel-based radial basis function extreme learning machine, Chaos Solitons Fractals 199 (2025) 116751, https://doi.org/10.1016/j.chaos.2025.116751.
[35] K. Sada, Y. Miyawaki, R. Yanai, T. Kida, A. Onishi, R. Yoshimi, K. Ichinose, Y. Shimojima, Development and validation of data-driven, decision tree–based algorithms for identifying behçet's disease in claims data, Int. J. Med. Inf. 209 (2026) 106266, https://doi.org/10.1016/j.ijmedinf.2026.106266.
[36] Z. Sun, G. Wang, P. Li, H. Wang, M. Zhang, X. Liang, An improved random forest based on the classification accuracy and correlation measurement of decision trees, Expert Syst. Appl. 237 (2024) 121549, https://doi.org/10.1016/j.eswa.2023.121549.
[37] L. Rokach, O. Maimon. Data mining with decision trees: theory and applications, 2nd ed, World Scientific Publishing Co., Inc., New Jersey, 2014.
[38] X. Duan, H. Xu, E. Wang, C. Guo, Z. Fang, T. Yang, Y. Zhao, X. Hou, Design of novel Ni-based superalloys with better oxidation resistance with the aid of machine learning, J. Mater. Sci. 58 (2023) 11100–11114, https://doi.org/10.1007/s10853-023-08712-z.
[39] X. Sun, L. Zhang, Y. Pan, Z. Huang, L. Jiang, Investigation of breakaway oxidation kinetics of nickel-base single crystal superalloys: modeling and experiments, Mater. Today Commun. 32 (2022) 103893, https://doi.org/10.1016/j.mtcomm.2022.103893.
[40] X. Sun, L. Zhang, Y. Pan, L. Zhu, Z. Huang, L. Jiang, Tuning Mo/W ratio to improve high temperature oxidation resistance of single crystal nickel base superalloys, Mater. Today Commun. 38 (2024) 107826, https://doi.org/10.1016/j.mtcomm.2023.107826.
[41] J.L. Smialek, P.J. Bonacuse, Compositional effects on the cyclic oxidation resistance of conventional superalloys, Mater. High. Temp. 33 (2016) 489–500, https://doi.org/10.1080/09603409.2016.1160501.
[42] X. Sun, L. Zhang, Y. Pan, X. Wang, Z. Huang, L. Jiang, Microstructural evolution during cyclic oxidation of a Ni-based singe crystal superalloy at 1100 °C, Corros. Sci. 162 (2020) 108216, https://doi.org/10.1016/j.corsci.2019.108216.
[43] J.L. Smialek, Universal characteristics of an interfacial spalling cyclic oxidation model, Acta Mater. 52 (2004) 2111–2121, https://doi.org/10.1016/j.actamat.2004.01.032.
[44] J.L. Smialek, A deterministic interfacial cyclic oxidation spalling model, Acta Mater. 51 (2003) 469–483, https://doi.org/10.1016/S1359-6454(02)00430-5.
[45] C.S. Tedmon, The effect of oxide volatilization on the oxidation kinetics of Cr and Fe-Cr alloys, J. Electrochem. Soc. 113 (1966) 766–769, https://doi.org/10.1149/1.2424115.

[46] Z. Zhang, R.F. Webster, J. Zhang, Alloying effects of Al, Si and Fe on Ni-20Cr alloy oxidation in water vapour at 650 °C, Corros. Sci. 232 (2024) 112050, https://doi.org/10.1016/j.corsci.2024.112050.
[47] D.J. Young, High temperature oxidation and corrosion of metals, Elsevier, 2016, https://doi.org/10.1016/C2014-0-00259-6.
[48] T.D. Nguyen, J. Zhang, D.J. Young, Growth of Cr_2O_3 blades during alloy scaling in wet CO_2 gas, Corros. Sci. 133 (2018) 432–442, https://doi.org/10.1016/j.corsci.2018.01.045.
[49] J. Stringer, The reactive element effect in high-temperature corrosion, Mater. Sci. Eng. A 120-121 (1989) 129–137, https://doi.org/10.1016/0921-5093(89)90730-2.
[50] K. Fritscher, The Reactive Element Effect, Metall. Mater. Trans. A 54 (2022) 64–74, https://doi.org/10.1007/s11661-022-06840-w.
[51] Z. Zhao, Effect of Y on Oxidation Behavior of Directionally Solidified Ni-Based Single-Crystal Superalloy, Chin. J. Mech. Eng. 37 (2024) 100.
[52] D. Naumenko, B.A. Pint, W.J. Quadakkers, Current thoughts on reactive element effects in alumina-forming systems: In memory of john stringer, Oxid. Met. 86 (2016) 1–43, https://doi.org/10.1007/s11085-016-9625-0.
[53] Q. Wang, Q. Wang, R. Chen, X. Wang, Y. Su, H. Fu, Optimizing isothermal oxidation behavior of the Y-containing Nb-Ti-Si based alloy: the role of precursor Y_2O_3, Corros. Sci. 227 (2024) 111706, https://doi.org/10.1016/j.corsci.2023.111706.
[54] S.-L. Shang, Y. Wang, B. Gleeson, Z.-K. Liu, Understanding slow-growing alumina scale mediated by reactive elements: perspective via local metal-oxygen bonding strength, Scr. Mater. 150 (2018) 139–142, https://doi.org/10.1016/j.scriptamat.2018.03.002.
[55] Y. Niu, X.J. Zhang, Y. Wu, F. Gesmundo, The third-element effect in the oxidation of Ni-xCr-7Al (x = 0, 5, 10, 15 at%) alloys in 1atm O_2 at 900-1000 °C, Corros. Sci. 48 (2006) 4020–4036, https://doi.org/10.1016/j.corsci.2006.03.008.
[56] F.H. Stott, G.C. Wood, The mechanism of oxidation of Ni-Cr-Al alloys at 1000°-1200 °C, Corros. Sci. 11 (1971) 799–812, https://doi.org/10.1016/S0010-938X(71)80044-6.
[57] F.H. Stott, G.C. Wood, M.G. Hobby, A comparison of the oxidation behavior of Fe-Cr-Al, Ni-Cr-Al, and Co-Cr-Al alloys, Oxid. Met. 3 (1971) 103–113, https://doi.org/10.1007/BF00603481.
[58] I.A. Kvernes, P. Kofstad, The oxidation behavior of some Ni-Cr-Al alloys at high temperatures, Metall. Trans. 3 (1972) 1511–1519, https://doi.org/10.1007/BF02643040.
[59] L. McInnes, J. Healy, N. Saul, L. Großberger, UMAP: uniform manifold approximation and projection, J. Open Source Softw. 3 (2018) 861, https://doi.org/10.21105/joss.00861.
[60] I. De Zarzà, J. De Curtò, C.T. Calafate, UMAP for geospatial data visualization, Procedia Comput. Sci. 225 (2023) 1661–1671, https://doi.org/10.1016/j.procs.2023.10.155.
[61] F.H. Stott, G.C. Wood, J. Stringer, The influence of alloying elements on the development and maintenance of protective scales, Oxid. Met. 44 (1995) 113–145, https://doi.org/10.1007/BF01046725.
[62] M.P. Brady, I.G. Wright, B. Gleeson, Alloy design strategies for promoting protective oxide-scale formation, JOM 52 (2000) 16–21, https://doi.org/10.1007/s11837-000-0109-x.
[63] X. Peng, D. Ping, T. Li, W. Wu, Oxidation behavior of a Ni-La_2O_3 codeposited film on nickel, J. Electrochem. Soc. 145 (1998) 389–398, https://doi.org/10.1149/1.1838274.
[64] A. Atkinson, R.I. Taylor, A.E. Hughes, A quantitative demonstration of the grain boundary diffusion mechanism for the oxidation of metals, Philos. Mag. A 45 (1982) 823–833, https://doi.org/10.1080/01418618208239905.
[65] Y. Qiu, J. Niu, C. Zhang, L. Chen, B. Su, S. Zhou, Interpretable machine learning reveals transport of aged microplastics in porous media: multiple factors co-effect, Water Res 274 (2025) 123129, https://doi.org/10.1016/j.watres.2025.123129.
[66] Z. Fu, X. Yang, Y. Ma, Y. Sun, T. Wang, Integrating explainable AI and causal inference to unveil regional air quality drivers in China, J. Environ. Manag. 390 (2025) 126270, https://doi.org/10.1016/j.jenvman.2025.126270.